Chen et al. *NPG Asia Materials* (2023) 15:34
https://doi.org/10.1038/s41427-023-00479-8

NPG Asia Materials

ARTICLE Open Access

Anomalous anisotropic magnetoresistance in the topological semimetal HoPtBi

Jie Chen[1,2], Hang Li[1], Tengyu Guo[2], Peng Chen[2], Dongfeng Zheng[2], Guoqiang Yu[2,3], Yong-Chang Lau[3,4], Xuekui Xi[3] and Wenhong Wang[1,2,3]

Abstract

Discovering and understanding anomalous anisotropic magnetoresistance (AMR) effects are important aspects of studying the nature of modulated transport. The anisotropic transport coefficients of topological systems are often useful for mapping hidden phases and characterizing topological phase transitions and the evolution of topological electrons. Here, we report an unusual change in the AMR effect in HoPtBi. Remarkably, the AMR exhibits transitions from a quasi-twofold to fourfold symmetry and finally forms a stable rotated fourfold symmetry with increasing magnetic fields. The evolution analysis from the three-dimensional (3D) mapping experiments confirms that it is an intrinsic 3D effect. Fourier transformation analysis indicates that the superposition of C_2, C_4, and C_6 signals with phase angle transitions leads to the novel AMR. All transitions are summarized as symmetry rotation or the inversion of peaks and valleys. By combining the features of band structures and AMR, we evaluate the possible origin of this symmetry rotation and attribute it to the topological band change. This work provides insight into the anomalous AMR effect of topological materials and is useful for understanding the evolution of topological bands in a magnetic field. We propose that other rare-earth half-Heusler alloys can potentially exhibit similar phenomena.

Introduction

Transport properties related to topological bands have received considerable attention in fundamental science and potential technological applications. The anisotropic transport coefficients of topological systems are often useful for the mapping of hidden phases with distinct symmetries[1]. For topological semimetals, topological bands, such as Dirac points, Weyl points and nodal lines, exhibit exciting physical properties[2–6]. In particular, these bands strongly influence the transport properties due to their ultrahigh carrier mobility[5,7] and strong Berry curvature[8–10]. The longitudinal resistivity based on topological materials is mostly related to large magnetoresistance[11], linear magnetoresistance[12], chiral-anomaly induced negative magnetoresistance[13,14], and the planar Hall effect[15,16]. In magnetic topological materials, unconventional magnetoresistance behavior is often observed when combining topological bands and magnetism. Anisotropic magnetoresistance (AMR) is an effective method to detect the symmetry of the Fermi surface[17,18], hidden phases[1,19], and topological phase transitions[20]. Generally, the angle-dependent magnetoresistance originates from the relativistic spin-orbit coupling (SOC) in magnetic materials, inherently determined by the variation in conductivity and density of states (DOS) at the Fermi level in a magnetic field[21]. The AMR symmetry is closely related to the symmetries of the crystal and magnetic sublattice. An abnormal AMR effect, including rotating AMR and symmetry breaking, has attracted research attention due to its great physics and potential applications[22]. The occurrence of this anomaly requires a phase transition, such as a metamagnetic transition, topological phase transition, or density of charge carriers, to modulate or break the symmetry, such as CeAlGe[1,23], CeSb/Bi[24,25], Sr_2IrO_4[26–29], and $EuTiO_3$

Correspondence: Wenhong Wang (wenhongwang@tiangong.edu.cn)
[1]School of Electronic and Information Engineering, Tiangong University, 300387 Tianjin, China
[2]Songshan Lake Materials Laboratory, 523808 Dongguan, Guangdong, China
Full list of author information is available at the end of the article

films[30]. However, an abnormal AMR in nonmagnetic ordering or nonmagnetic materials is quite rare.

Half-Heusler compounds, RPtBi, are a family of magnetic topological semimetals. They have attracted much attention due to their rich and excellent topological transport properties, such as giant anomalous Hall angle[31–39], large negative magnetoresistance induced by chiral anomalies[40–42], planar Hall effect[43], and thermoelectric effect[44]. Compared to the transport behavior of ferromagnetic or noncollinear antiferromagnetic topological semimetals, half-Heusler compounds usually exhibit unconventional behavior, such as a drum-like anomalous Hall effect[32,33,40], magnetic-field induced sign change of AHE[39], and abnormal planar AMR[15]. These anomalies indicate that the band of RPtBi is unstable in the presence of an external magnetic field. Previous theoretical calculations showed that the Zeeman energy[41] or an exchange field[31] split the band and led to crossing (Weyl points) around the Fermi level in a magnetic field. However, detailed characterization of the specific dynamic progress is difficult and has not been reported thus far because this effect is weak and appears in low magnetic fields; thus, the Fermi surface detection tool, the Shubnikov-de Haas (SdH) effect, does not occur. The AMR effect is sensitive to topological phase transitions, Fermi surface symmetry, and hidden phases and can provide good insight into the evolution of topological bands in a magnetic field and show the band modulation process of half-Heusler alloys from another perspective.

In this work, we thoroughly studied the AMR in HoPtBi with $B \perp I$, where B rotated in certain crystallographic planes. The AMR symmetry exhibited a dramatic change when B increased. Remarkably, B caused a change from twofold to fourfold AMR at low B, and as B increased, the magnetic field induced an AMR contour rotation of 45°. Further analysis via Fourier transformation (FT) indicated that the AMR originated from the contributions of C_2, C_4, and C_6 signals. In particular, C_2 and C_4 signals dominated the AMR and exhibited a phase angle transition, phenomenologically explaining the dramatic change in the AMR behavior. The 3D map analysis of the AMR further identified that the dramatic AMR change was a 3D effect. The results indicated that this phenomenon could originate from the topological band change in an external magnetic field.

Materials and methods

Sample preparation

Single crystals of HoPtBi were grown from high-purity starting materials (molar ratio Ho:Pt:Bi = 1:1:15) via a standard self-flux method[39]. The pure elements were placed in an alumina crucible. The whole tube was sealed in an evacuated quartz tube to prevent high-temperature oxidation. The crystal growth was as follows: first, the tube was heated from room temperature to 1150 °C and maintained at this temperature for one day, then slowly cooled to 650 °C at a rate of 2 K h^{-1}. The excess Bi flux was removed by centrifuging the tube at 650 °C. Bulk single crystals of HoPtBi with typical dimensions of 1.5 mm × 1 mm × 1 mm were obtained. The inset in Fig. S1b in the Supplementary information shows a photograph of the HoPtBi single crystal with the (111) plane.

Physical property characterization

The magnetic properties were measured in a Quantum Design Magnetic Property Measurement System (7 T, MPMS 3). The magnetotransport measurement was carried out based on the four-probe method in a Physical Property Measurement System (9 T, PPMS) with a sample rotator and a Cryogen-Free Magnet System with a 3D rotating magnetic field. The magnetic torque measurement was carried out on the PPMS with the Torque Magnetometer. The upper limit of torque is 10^{-5} Nm. The crystal structure of single crystals was characterized via a Rigaku XRD system with Cu K_α radiation ($\lambda = 1.5418$ Å) at room temperature.

First principle calculations

The density of states (DOS) was calculated using the WIEN2K code based on the framework of density functional theory[45]. The Perdew-Burke-Ernzerhof generalized gradient approximation[46] was used to calculate exchange correlation potentials. The cutoff energy was set to −6.0 Ry, defining the separation of the valence and core states. Due to heavy elements, we included spin-orbit coupling (SOC) in a second variational procedure. A large exchange parameter, $U_{eff} = 0.6$ Ry, was applied to Ho. The Fermi surface was plotted with the *XCrysDen* program.

Results

Anomalous AMR with *B* rotating in the (100) and (110) planes

From Fig. 1a, HoPtBi crystallizes in a noncentrosymmetric cubic structure with a space group F-43m. The Néel temperature is 1.2 K[35], and there are no traces of metamagnetic transitions in the paramagnetic state[39]. The resistivity ρ_{xx} (0 T) exhibits semiconductor to metal-like behavior (Fig. S1a). The red planes in Fig. 1a and d are the (100) and (110) planes, respectively. In configuration **I** (inset in Fig. 1b), B rotates in the (100) plane, I along [100] direction, and B and I remain perpendicular. Figure 1b shows the angular dependence of ρ_{xx} (B), and Fig. 1c represents the AMR curves at several typical magnetic fields for configuration **I**. Clearly, the ρ_{xx} (B) curves show a small change at $B \leq 1$ T at different angles. The AMR curve at 0.7 T shows weak anisotropy and exhibits an approximate twofold symmetry (Fig. 1c). The peak position is approximately 90°. With increasing B, the ρ_{xx} (B)

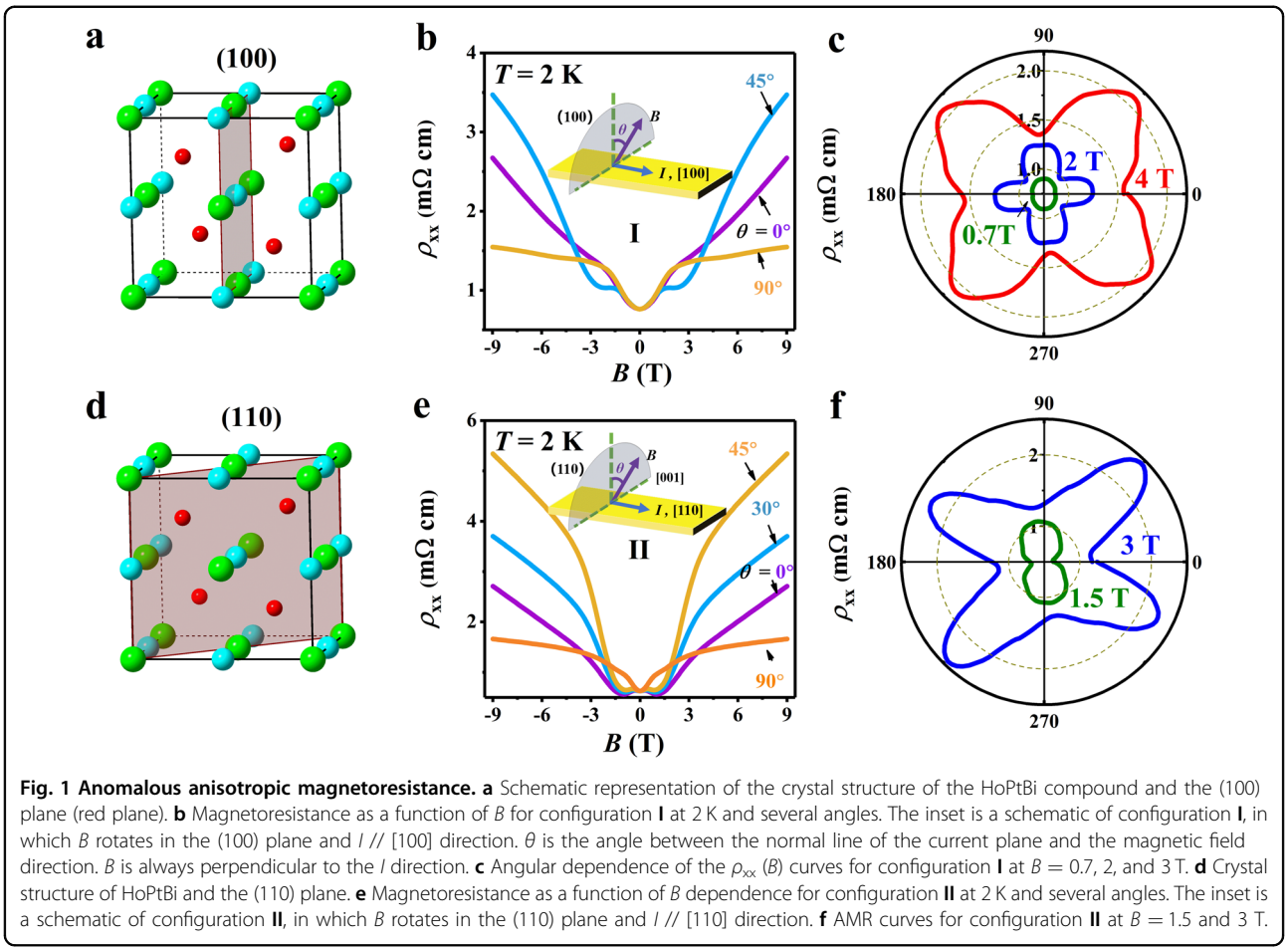

Fig. 1 Anomalous anisotropic magnetoresistance. a Schematic representation of the crystal structure of the HoPtBi compound and the (100) plane (red plane). **b** Magnetoresistance as a function of *B* for configuration **I** at 2 K and several angles. The inset is a schematic of configuration **I**, in which *B* rotates in the (100) plane and *I* // [100] direction. *θ* is the angle between the normal line of the current plane and the magnetic field direction. *B* is always perpendicular to the *I* direction. **c** Angular dependence of the ρ_{xx} (*B*) curves for configuration **I** at $B = 0.7$, 2, and 3 T. **d** Crystal structure of HoPtBi and the (110) plane. **e** Magnetoresistance as a function of *B* dependence for configuration **II** at 2 K and several angles. The inset is a schematic of configuration **II**, in which *B* rotates in the (110) plane and *I* // [110] direction. **f** AMR curves for configuration **II** at $B = 1.5$ and 3 T.

curves of $\theta = 0°/90°$ and $\theta = 45°$ separate at about $B = 1$ T. The AMR symmetry becomes a fourfold contour at 2 T. It forms peaks in the *B* // [100] direction (90°) and turns to a valley in the *B* // [110] direction (45°). At high *B*, the ρ_{xx} (*B*) curve of $\theta = 45°$ is enhanced. At $B = 4$ T, the AMR symmetry is rotated by approximately 45° such that the peaks of the fourfold AMR shift from the [100] to [110] direction. These results indicate that the HoPtBi single crystal has a complex magnetic-field-induced AMR effect.

The MR line types at different angles also show strong anisotropy. Figure S5 provides the polynomial fitting of MR at $\theta = 0°$ and 45°. The MR in $B < 1$ T shows similar behavior, which is consistent with the weak anisotropy of AMR. In the range of $1\text{ T} < B < 3\text{ T}$, the MR cannot be scaled by the linear and quadratic terms, which is potentially related to the band change, a phenomenon similar to that observed in $ZrTe_5$ with topological phase transition[20]. Notably, the change in AMR symmetry occurs in this magnetic field range. The line types in a high magnetic field also show different behaviors in that the quadratic term changes sign. Remarkably, the Berry phase at high magnetic fields also shows distinct changes at $\theta = 0°$ (*B*//[100]) and 45° (*B*//[110]) (Fig. S17). A nontrivial Berry phase is taken at *B*//[100], but a value (-0.4π) other than π is taken at *B*//[110]. Thus, the symmetry rotation at 4 T is potentially related to the anisotropy of the Berry phase and topological properties.

In configuration **II** (inset in Fig. 1e), I // [110], *B* rotates in the (110) plane, and *B* and *I* also remain perpendicular. We select several angles to assess the *B*-dependence of ρ_{xx} (*B*) (Fig. 1e). The ρ_{xx} (*B*) curves exhibit distinctly different *B*-dependent behavior for high and low fields. In a weak magnetic field, ρ_{xx} ($\theta = 90°$) shows V-type curves, unlike those at $\theta = 0$, 30, and 45°. Correspondingly, a twofold symmetry AMR at 1.5 T is formed with a peak along [100] (90°) in Fig. 1f. In a high magnetic field, ρ_{xx} ($\theta = 45°$) is enhanced, and the four-peak feature is stable at $B \geq 3$ T (Fig. S10g).

In the supplemental materials (SM), Fig. S10 shows the AMR results for configuration **III**. The abnormal AMR phenomenon also appears. These results indicate that the abnormal AMR effect is not accidental. The magnetic field rotates in the (110) plane and current *I* // [110] in configurations **II** and **III**. The difference is that *I* is along the (111) plane for configuration **II**, and *I* is along the

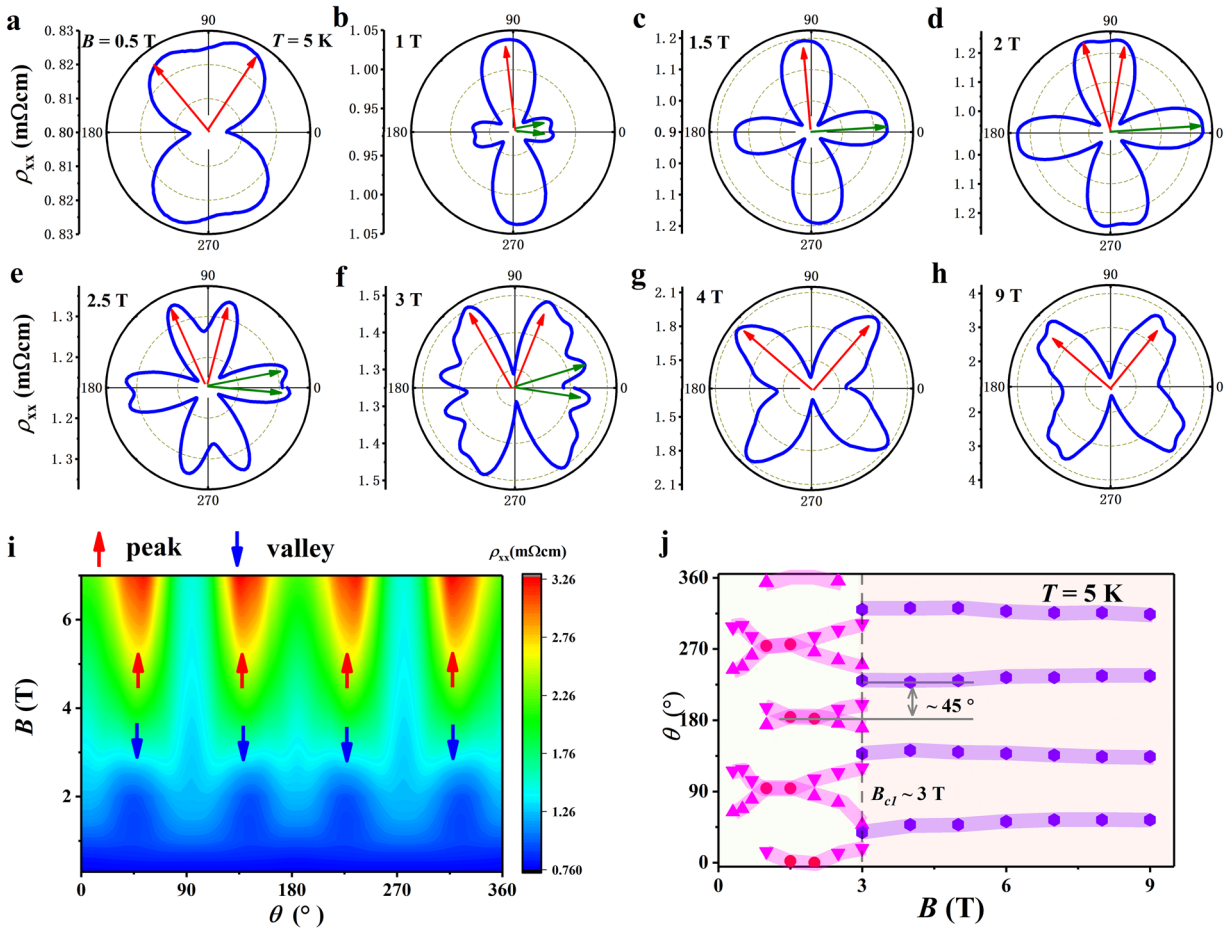

Fig. 2 Detailed AMR curves for configuration I with *B* rotating in the (100) plane, *I* // [100] direction, and *T* = 5 K. a–h Featured AMR curves at different magnetic fields. **i** AMR map collected under a series of magnetic fields at 5 K. The blue arrow is the valley of MR, and the red arrow is the peak of MR. **j** Peak position of the AMR curves in (**a**) as a function of *B*, in which the rotated fourfold AMR is formed at B_{c1}. The relative shift between two fourfold MRs is approximately 45°.

(110) plane for configuration **III**. If the AMR signal depends on the crystal symmetry, then a certain angle will appear between the two samples. The rotation angle between the two samples is approximately 36°, which is consistent with the geometrical relationship between the (111) and (110) planes (see Fig. S10d, e), indicating the crystal-axis dependence of the AMR. The abnormal AMR effect with *B* rotating in the (100) and (110) planes indicates a possible three-dimensional (3D) effect.

Magnetic field dependence of the abnormal AMR in configuration I

We performed comprehensive AMR characterization for configuration **I** at a series of magnetic fields to reveal the *B*-dependent AMR behavior. The detailed results of AMR at 5 K are shown in Fig. 2. Here, the curves with the typical features show the AMR evolution. Figure 2a–h shows the shape of the AMR at different magnetic fields. At $B = 0.3$ T, the twofold symmetry curve is formed, and the slightly splitting peak approaches 90°. As *B* increases, a small double-peak signal appears at approximately 0° and $B = 1$ T (Fig. 2b), the amplitude of which increases as *B* increases up to 2 T (Fig. 2d). In this process, the double-peak feature gradually disappears and forms a large peak. As *B* continually increases, the large peak splits into a double-peak signal and gradually shrinks (Fig. 2d–f). This progress is stronger at 2 K in Fig. S3. In the range of high magnetic fields, this signal around 0° disappears completely. Interestingly, the peak at 90° begins to split into two peaks at approximately 2 T (Fig. 2d). The splitting peaks completely separate as *B* increases, and they become stable at approximately 45 and 135°. At high magnetic fields, the fourfold symmetry of the AMR curves with a peak at 45° only persists (Fig. 2g, h).

Figure 2i maps the AMR effect at $T = 5$ K and 0.3 T ≤ *B* ≤ 7 T. The color contrast indicates the change in ρ_{xx} (*B*). The fourfold AMR transition is clear at approximately 3 T. Another feature in the mapping is a twofold

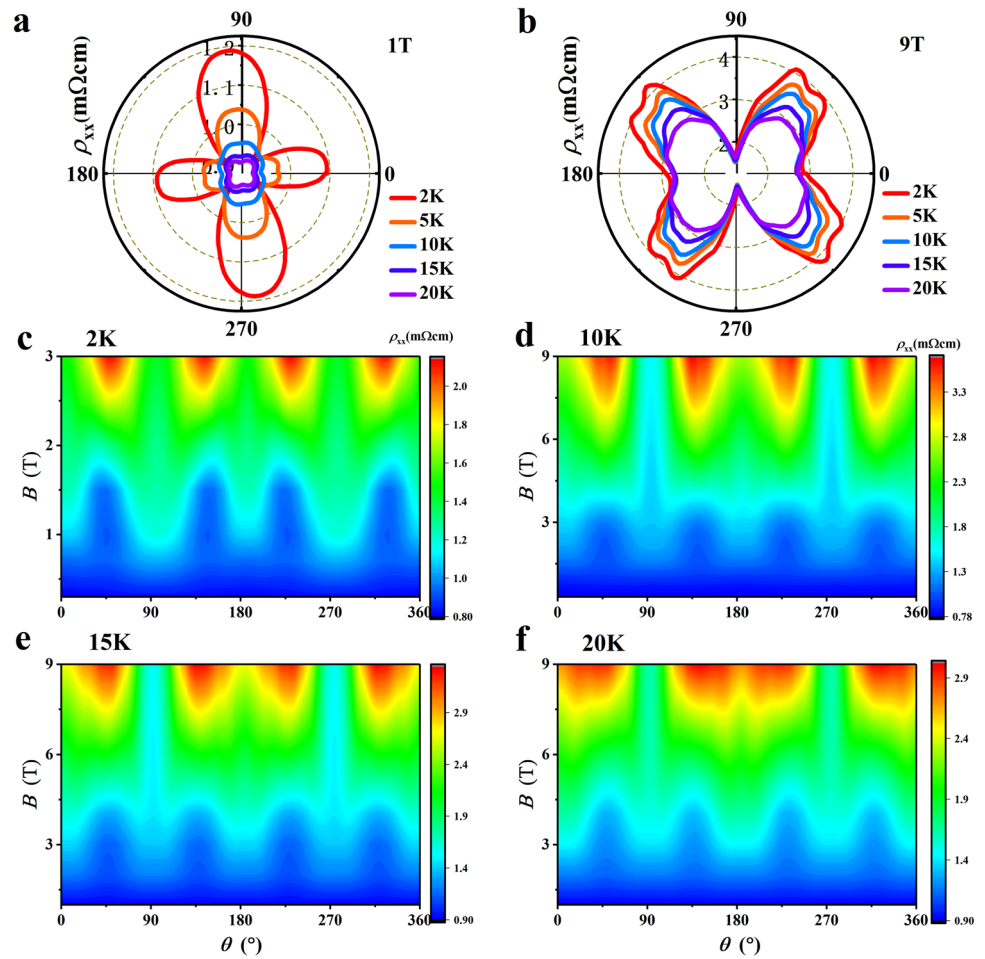

Fig. 3 Detailed *T*- and *B*-dependent AMR curves for configuration I with *B* rotating in the (100) plane, *I* // [100] direction. (**a**) and (**b**) are the AMR curves at 1 and 9 T, respectively. **c**–**f** AMR maps collected under a series of magnetic fields at 2, 10, 15, and 20 K. The blue arrow is the valley of MR, and the red arrow is the peak of MR.

symmetry of the AMR signal with the pale blue color, crossing the high magnetic field at $B \geq 3$ T, which is distinguished from that at 0.7 T in Fig. 1c. The valley of the twofold symmetry AMR at high magnetic fields rotates 90° compared to that at low magnetic fields. To clearly show the AMR evolution, the peak positions formed in the phase diagram of AMR in Fig. 2j are used. The symmetry of the AMR exhibits a dramatic change at $B \leq 3$ T and $T = 5$ K. For $B \leq 3$ T, the peaks around 0 and 90° independently evolve as B increases. Phenomenologically, the split peaks merge into a single peak at 1 T, then split again and form a rotated fourfold AMR at $B \geq 3$ T. The rotation degree between the fourfold AMR at 1.5 T and the fourfold AMR at $B \geq 3$ T occur approximately 45°.

Temperature dependence of the abnormal AMR effect in configuration I

In Fig. 3, we show the temperature dependence of the AMR map ($T \leq 20$ *K*) in configuration **I**. Considering the significant difference between low B and high B, the temperature dependence AMR curves at 1 and 9 T are illustrated in Figs. 3a and b, respectively. When $B = 1$ *T*, the fourfold AMR with a peak along the [100] direction is observed at $T = 2$ *K* and 5 K. When $T \geq 10$ *K*, 1 T can induce only a quasi-twofold AMR as T increases. When $B = 9$ *T*, a stable AMR contour and the rotated fourfold AMR with a peak along the [110] direction appear at $T \leq 20$ *K*. Remarkably, ρ_{xx} (B) in the [100] direction remains almost unchanged as T increases, while ρ_{xx} (B) in the [110] directions decreases with increasing T. This significant difference in temperature-dependent properties indicates possibly different magnetoresistance mechanisms at high fields. Figure 3c–f map the AMR effect at $T = 2$, 10, 15, and 20 K. The critical field required for forming the rotated fourfold AMR is defined as B_{c1}. The critical field for reversing the fourfold AMR increases with T. Figure S4 shows the temperature dependence of B_{c1}. B_{c1} increases smoothly with T when $T \leq 20$ *K*. Thus, the

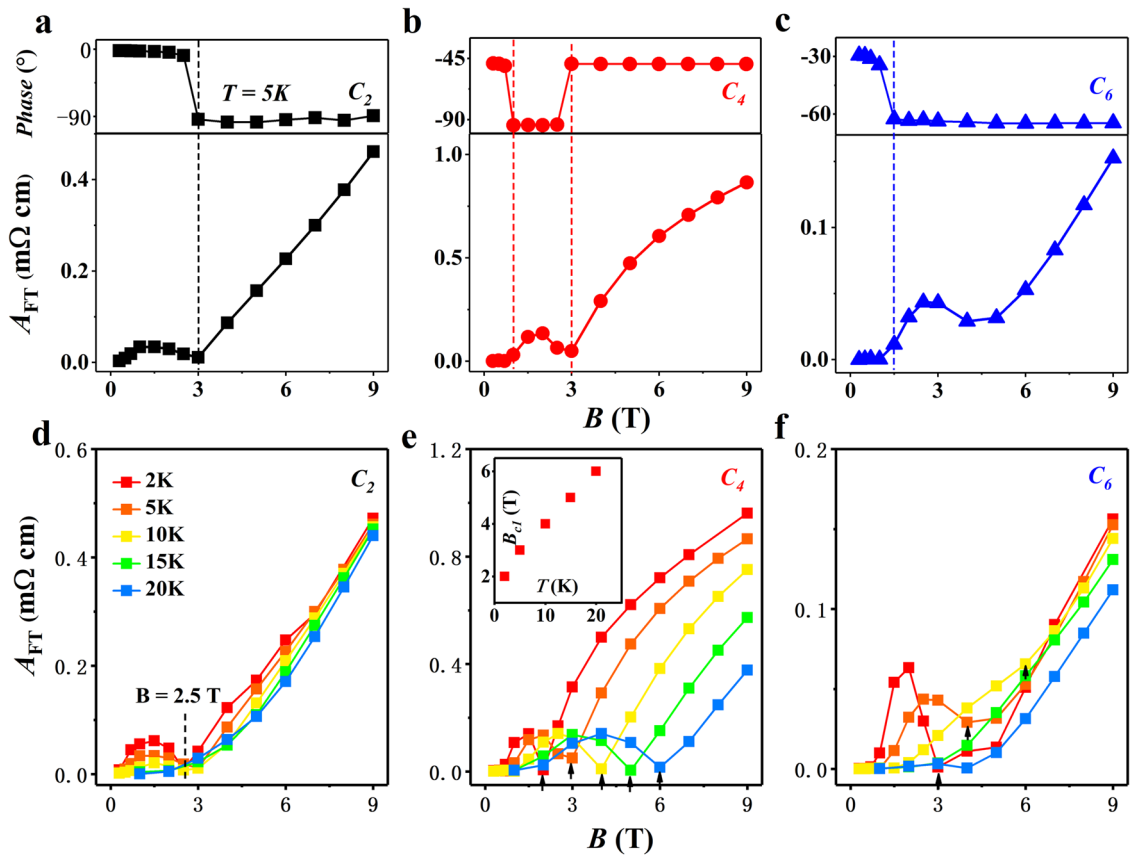

Fig. 4 Extracted FT amplitude and phase angle for configuration *I* with *B* rotating in the (001) plane. a–c Magnetic field dependence of the FT amplitude A_{FT} and phase angle for C_2, C_4, and C_6 signals at 5 K. **d–f** Magnetic field dependence of $A_{FT}(C_2)$, $A_{FT}(C_4)$, and $A_{FT}(C_6)$ at different temperatures, respectively. The inset in Panel (**e**) is the temperature dependence of the critical field B_{c1} for the C_4 transition at high magnetic fields.

complex AMR behavior with B rotating in the (100) plane is confirmed.

Mechanism of the complex AMR behavior

The previous section clarifies the unusual AMR behavior. However, the mechanism behind the phenomenon is still elusive since the mixture of the AMR signals with different symmetries causes further quantitative analysis to be challenging. Fourier transformation is an effective analytical tool for analyzing periodic signals, causing the complex AMR behavior, symmetry, and phase angle transition of AMR curves to become clearer. Thus, we perform FT analysis of the AMR in configuration **I**. Figure S12b shows the period (ω) of the FT amplitude (A_{FT}) at 5 K. ω is the reciprocal of the FT frequency. Three signals with periods $\omega = 180$, 90, and 60° dominate the AMR curves, corresponding to C_2, C_4, and C_6 symmetry, respectively. Here, we extract the A_{FT} and phase angle as functions of B. Figure 4a–c shows the magnetic field dependence of the phase and A_{FT} for C_2, C_4, and C_6 in configuration **I** at 5 K. The phase and A_{FT} of C_2, C_4, and C_6 signals strongly depend on B. First, we select the C_2 signal to show the evolution. The $A_{FT}(C_2)$ can be divided into two sections (Fig. 4a). In the low-magnetic field range ($B < 3$ T), $A_{FT}(C_2)$ initially increases and then decreases to almost zero at 3 T. In the high-magnetic field range ($B > 3$ T), $A_{FT}(C_2)$ monotonically increases. Along with this progress, the phase angle of the C_2 signal shows an abrupt switch from 0 to 90° at the critical field, indicating that the twofold symmetry of the AMR signal rotates 90°. The switch indicates a possible band change. However, this kind of transition is not an isolated phenomenon. The phase angles of the C_4 and C_6 signals also show abrupt transitions in the low B range. The contribution of the C_4 signal can be divided into three sections, as shown in Fig. 4b. In low- and high-magnetic field ranges, the phase angle is 45°. In the middle range, the phase angle shifts to 90°, and the fourfold symmetry of the AMR signal rotates 45° in this range. The critical fields of the two transitions are 1 and 3 T. The $A_{FT}(C_4)$ also swells in the middle range. Remarkably, in the same range, a Hall resistivity well forms with B // [100][39] in Fig. S6a, and this anomaly is usually ascribed to the Berry curvature-induced AHE for half-Heusler systems[31,32,39,40]. Remarkably, the Hall

resistivity exhibits a sign change between the B // [100] and B // [110] directions[39] (Fig. S6). This result indicates that the system can potentially undergo a topological band change for different directions of the magnetic fields. All transitions of the three signals are summarized as the symmetry rotation or the inversion of the peaks and valleys. By comparing the A_{FT} values of the three signals (see Fig. S12), the C_4 signal dominates, followed by C_2, while the contribution of the C_6 signal is negligible. The complex AMR behavior is divided into three symmetrical signals, exhibiting three typical features. First, the phase angle shows sharp transitions at low magnetic fields. Second, coupled to the phase angle transition, the A_{FT} amplitude shows a nonpolynomial variation with B. Third, the critical magnetic fields of the three signals are independent, indicating that different symmetrical signals are nonuniform magnetic responses. In the high-magnetic field range, the phase angles of all signals remain stable, and the A_{FT} continues to increase monotonically.

The temperature evolution of the three signals is also extracted from the FT of the AMR. Figure 4d–f show the B-dependence of the A_{FT} for C_2, C_4, and C_6 signals at different T. The $A_{FT}(C_2)$ signal peak decreases with T in the low-magnetic field range. The swell almost disappears at 10 K. Interestingly, the critical field of the transition is stable at approximately 2.5 T for $T < 10$ K. Above the critical field, $A_{FT}(C_2)$ decreases slowly with T. In contrast, the C_4 signal exhibits a different temperature dependence. First, the peak of the $A_{FT}(C_4)$ swell is stable at different T. However, the magnetic field range of the swell extends, and the critical field B_{c1} increases with T. Second, the $A_{FT}(C_4)$ value above B_{c1} decreases monotonically with T. The similar behavior of B_{c1} in Fig. 4 and the inset in Fig. 4e indicates that the progress extracted by FT is reliable and that the C_4 signal dominates the abnormal AMR behavior at low magnetic fields. For the C_6 signal, the peak of the $A_{FT}(C_6)$ swell decreases and gradually disappears at 10 K. The $A_{FT}(C_6)$ above the swell slightly decreases with T. Compared to the C_2 and C_6 signals, the C_4 signal is more sensitive to the external field, including T and B.

3D mapping of the complex AMR behavior for configuration I

After the evolution of the novel AMR effect in two dimensions (2D) was resolved, so how does it evolve in the three -dimensional (3D) magnetic field? We constructed detailed 3D AMR maps at $T = 2$ K and a series of magnetic fields to characterize the exotic AMR effect more comprehensively. Figure 5d–f are 3D AMR maps at $B = 0.5$, 1, and 2 T, respectively. At $B = 0.5$ T, the AMR contour profile around $\varphi = 90°$ exhibited quasi-twofold symmetry, which was consistent with the 2D measurement in Fig. S4. From an overall perspective, there was a splitting tendency of the orange region from a twofold symmetry to a fourfold symmetry. At 1 T, the fourfold contour profile was formed at approximately $\varphi = 90°$ (Fig. 5e). Typical curves with $\varphi = 70°$ and 90° are shown in Fig. 5b. At 2 T, the orange region further split into 2 × 2 dots. Here, two typical AMR curves were used to show the changes in Fig. 5c. When $\varphi = 90°$, the AMR showed two small peaks at approximately $\theta = 0°$ and two large peaks at approximately $\theta = 90°$. When φ deviated from 90°, the two small peaks disappeared immediately, and the two large peaks were enhanced. From the 3D AMR maps, we observed the reconstruction progress of the AMR from a twofold at 0.5 T to a quasi-fourfold symmetry at 1 T, followed by further splitting at 2 T. These results indicated that the exotic AMR phenomenon in HoPtBi was a 3D effect and not only in a certain crystallographic plane. Research studies on Sr_2RuO_4 indicated that both the size and shape of the Fermi surface could be extracted from angular magnetoresistance oscillation measurements, which was consistent with those determined based on more rigorous quantum oscillation data[47–49]. The orbital AMR and the Fermi surface exhibited a close relationship. Therefore, as a powerful tool to detect the Fermi surface symmetry of 3D and quasi-2D systems[50], the AMR provided direct information on the Fermi surface at low magnetic fields. The AMR transition occurring at low field could correlate to the reconstruction of the Fermi surface.

Fermi surface topology and density of states

In this section, due to the close relationship between the orbital AMR and the Fermi surface, we show the Fermi surfaces and density of states (DOS) of HoPtBi. Figure S14 shows the band structures of HoPtBi in paramagnetic and ferromagnetic states. The bands crossing the Fermi level are indexed as 34, 35, and 36. The corresponding Fermi surfaces are shown in Fig. 6d. Figure S15 also provides the Fermi surfaces in the first Brillouin zone. The FT analysis indicates that there are three contributions, i.e., C_2, C_4, and C_6 signals, to the AMR. According to the relationship of the symmetry of AMR signals and the Fermi surface, the AMR symmetry is consistent with the Fermi surface in a certain plane. The Fermi surfaces of bands 34 and 35 show an approximate cubic structure, which is potentially related to the C_4 signal. Band 36 forms the Fermi surface with a sixfold disk and triangular columns on both sides of the disk, which potentially contributes to C_2 and C_6 signals. Based on the twofold magnetic anisotropy of HoPtBi in the (100) plane (Figs S8, S9), the C_2 signal may also contain a contribution from anisotropic magnetic scattering.

An important feature for the magnetic half-Heusler compound is magnetic field-induced band change. The nontrivial Berry phase extracted from SdH oscillations in

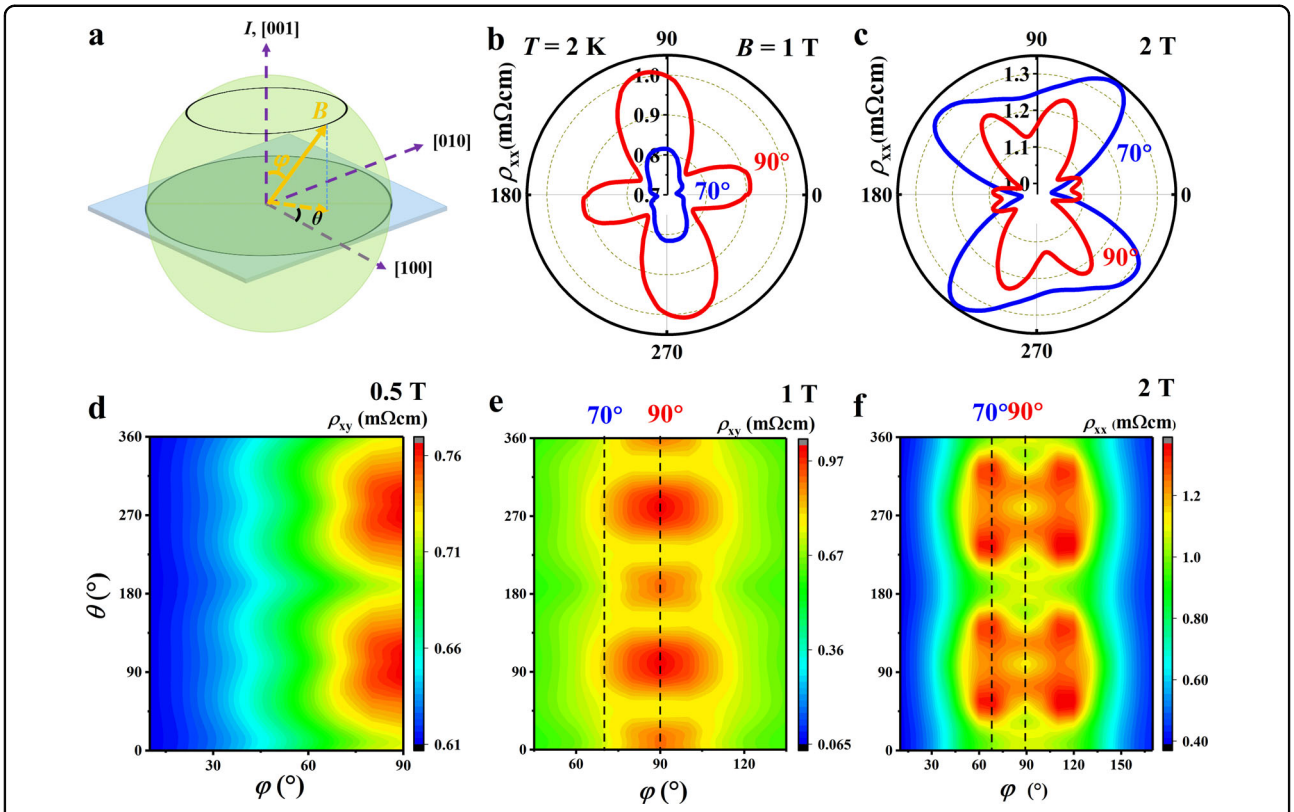

Fig. 5 3D mapping of AMR at 2 K. a Configuration of the 3D AMR measurement, *I* // [001] and *B* rotation in 3D space. The direction of *B* is defined by combining θ and φ. **b** AMR curves with $\varphi = 90$ and 70° at 1 T. The dashed lines in Panel (**e**) show the positions of 3D mapping. **c** MR curves with $\varphi = 90$ and 70° at 2 T. The dashed lines in Panel (**f**) show the positions of 3D mapping. **d**–**f** are detailed angular spectroscopic mapping of MR at 0.5, 1 and 2 T.

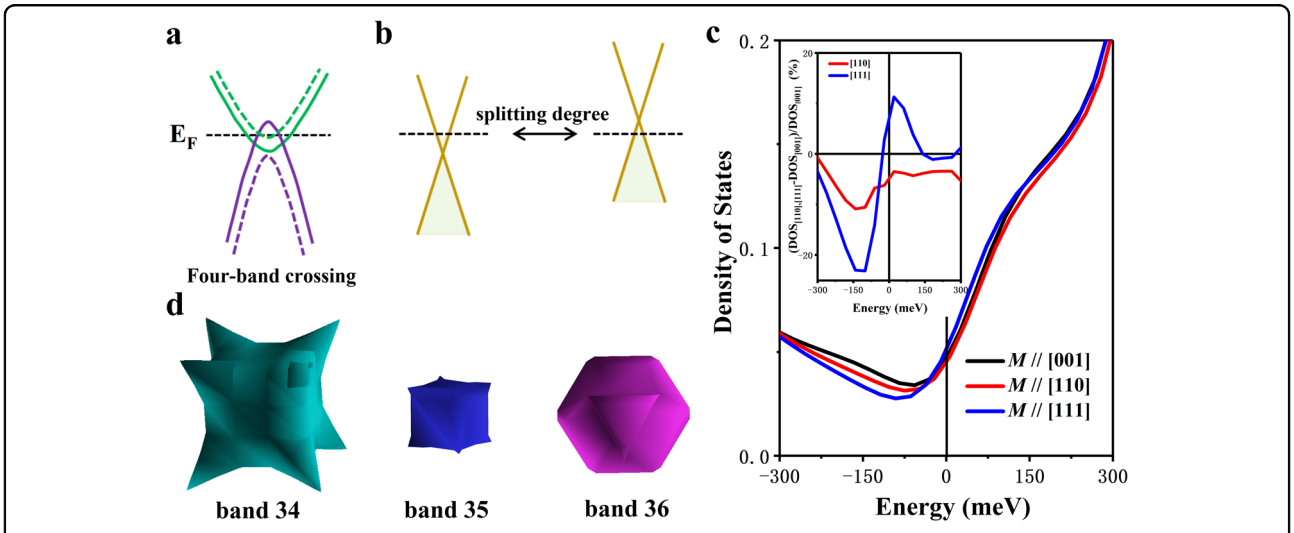

Fig. 6 Fermi surfaces and density of states of HoPtBi. a Schematic of the four-band crossing of the HoPtBi compound. **b** Positions of the band crossing tuned by the splitting degree. **c** Fermi surfaces for the three bands crossing the Fermi level with the magnetic moment along the [001] direction. **d** Density of states for *M* // [001], [110], and [111]. The inset is the relative change of *M* // [110] and [111] from the $DOS_{[001]}$.

high magnetic fields identified topological properties of HoPtBi (Fig. S17). In our study, the tunable effect of the external magnetic field on the bands is divided into two aspects: the intensity of band splitting and anisotropy. First, Fig. 6a shows a sketch of the four-band crossing at the Γ point. A magnetic field drives band splitting via Zeeman energy[41] or an exchange field[31]. In this process, the position and number of Weyl points are tuned by the intensity of external magnetic fields (Fig. 6b and Fig. S16). Figure S14 provides the band structures of paramagnetic and ferromagnetic states to simulate this process. Second, Fig. 6c shows the DOS of the HoPtBi compound with a magnetic moment along [001], [110], and [111]. It has a low DOS at E_F. The relative change in DOS with M // [111], [110] is approximately 5–10% to M // [001] (inset in Fig. 6c). This result correlates to an anisotropic tunable effect of magnetic fields on the bands. The theoretical calculations on GdPtBi[31] and HoPtBi[39] indicate that the position and number of Weyl points are also anisotropic for different moment directions. In our previous work on HoPtBi, the anisotropic additional Hall resistivity[39] also identified this fact (Fig. S6). In addition, the Berry phase also shows strong anisotropy at high magnetic fields. As shown in Fig. S17, the nontrivial π-Berry phase is extracted at B // [100], but a value (-0.4π) other than π is taken at B // [110]. This indicates that HoPtBi has a strong anisotropy of topological properties with B rotating in the (100) plane. The rotated fourfold AMR at high magnetic fields is potentially related to the anisotropy of the Berry phase. The band is dynamic with moment M rotating in a certain plane, and the magnetic field-induced variation also contributes to AMR. Therefore, the source of the phase angle transition can be related to the modulation of topological bands by the strength and direction of B.

Discussion

In our measurements, the AMR was measured in the configuration of B perpendicular to I. In practical measurements, a mismatch between the directions of B and I is inevitable, i.e., the directions of B and I are not strictly perpendicular, which yields a non-90° fixed angle between B and I. However, the 3D measurements of AMR in Fig. 5 show that the novel phenomenon is a 3D effect and intrinsic for HoPtBi.

The marked feature of HoPtBi is the dramatic change in the AMR at low fields. This transition shows a smooth change as B increases. The complex transitions of AMR were decomposed into three different symmetry signals with certain phase transformations using FT analysis. The anomaly at low fields is effectively shown and related to the anomalous phenomenon of the topological band change. In this section, the specific mechanism of phase angle transitions is discussed. First, as elaborated in the introduction, a metamagnetic transition accompanied by changing magnetic anisotropy is predominantly the key trigger of abnormal AMR. However, in the HoPtBi compound, the magnetic ordering temperature is $T_N = 1.2$ K[35]. All measurements were performed in paramagnetic states. To exclude the metamagnetic transition as the origin of the AMR transition, we made a comparison with the AMR change and magnetic anisotropy in same plane at 2 K and 5 K. In general, the symmetry change of AMR induced by meta-magnetic transitions should company with the symmetry change of anisotropic magnetization. As shown in Figs. S8 and S9, the highly sensitive magnetic torque measurement with B rotating in the (100) plane does not show any sign of magnetic anisotropy changes at $B \leq 2$ T. Therefore, the metamagnetic transition is excluded as the origin of phase angle transitions; specifically, there must be another special factor responsible for the novel phenomenon. Second, the modulation of the topological band also induces an anomalous AMR effect[18,20,51]. In the results section, we identified the topological band change under magnetic fields. At high magnetic fields, the stable rotated fourfold AMR is correlated with the anisotropy of topological bands and the Berry phase. At low magnetic fields, the absence of SdH prevents the detection of information on the Fermi surface and topological band change via SdH oscillations. However, the line-type change and the sign change of anomalous Hall at low magnetic fields indicate that the topological band change occurs and exhibits strong anisotropy. In topological materials, the positions of Weyl or Dirac points related to E_F usually strongly influence the transport properties[2,3], including chiral anomaly[52], AMR[51], and AHE[39,53]. Research on $BiSbTeSe_2$ nanodevices[51] provides another possible path to explain the phase angle transitions, indicating that shifting E_F up and down to the Dirac point by the applied gate voltage can switch the peaks and valleys of the AMR. Instead of the gate voltage, the magnetic field is the main factor that regulates the topological band in HoPtBi. The split of the four bands around E_F forms the band crossing and the shift of crossing around E_F in an external magnetic field and the modulated anisotropy of different bands. Therefore, the inversion of AMR peaks and valleys or the phase angle transitions in HoPtBi is deduced by modulating the position of the Weyl point crossing E_F. Another important feature of this mechanism is the critical field. The AMR transition in $BiSbTeSe_2$ nanodevices requires a critical gate field to shift the E_F crossing Dirac point. From the FT analysis, the C_2, C_4, and C_6 signals also show a critical field to shift the phase angle. All results indicate that the magnetic field-modulated topological bands are the origin of this novel AMR phenomenon.

Conclusion

We found an unusual AMR effect in the topological semimetal HoPtBi, indicating the modulation of the

topological band change. Since most of the AMR effects were stable and the symmetry was unchanged, the AMR with complex transitions was rare and usually underwent hidden phase transitions or symmetry breaking. The AMR of HoPtBi exhibited a dramatic change from a quasi-twofold symmetry to a fourfold symmetry and finally became a stable rotated fourfold symmetry as B increased. Further measurements identified that the abnormal AMR phenomenon in a low-magnetic field was an intrinsic 3D effect. From the FT analysis, we decomposed the complex AMR behavior into three different symmetrical signals. The AMR anomaly was ascribed to the composition of nonuniform phase angle transitions. Further analysis indicated that this phenomenon originated from the modulation of the topological band, including the formation of band crossing and the shift of crossing around E_F in an external magnetic field. Our results showed the rich physics of HoPtBi. In addition to HoPtBi, other rare-earth-based half-Heusler compounds could potentially exhibit similar unusual phenomena.

Acknowledgements
This work was supported by the National Key R&D Program of China (No. 2022YFA1402600), the National Science Foundation of China (Grants No.11974406 and No. 12074415), and the Strategic Priority Research Program (B) of the Chinese Academy of Sciences (CAS) (XDB33000000).

Author details
[1]School of Electronic and Information Engineering, Tiangong University, 300387 Tianjin, China. [2]Songshan Lake Materials Laboratory, 523808 Dongguan, Guangdong, China. [3]Beijing National Laboratory for Condensed Matter Physics, Institute of Physics, Chinese Academy of Sciences, 100190 Beijing, China. [4]University of Chinese Academy of Sciences, 100049 Beijing, China

Author contributions
J.C. and W.W. conceived the study and explained the experimental results. J.C. synthesized the single crystal. J.C., H.L., P.C., T.G., and D.Z. measured the physical properties of the single crystal. J.C. and W.W. analyzed the data and prepared the manuscript. All authors were involved in the discussion of the results and approved the final version of the manuscript.

Conflict of interest
The authors declare no competing interests.

Supplementary information The online version contains supplementary material available at https://doi.org/10.1038/s41427-023-00479-8.

Received: 21 November 2022 Revised: 5 April 2023 Accepted: 14 April 2023.
Published online: 19 May 2023

References

1. Suzuki, T., Savary, L., Liu, J.-P., Lynn, J. W., Balents, L. & Checkelsky, J. G. Singular angular magnetoresistance in a magnetic nodal semimetal. *Science* **365**, 377–381 (2019).
2. Collaudin, A., Fauqué, B., Fuseya, Y., Kang, W. & Behnia, K. Angle dependence of the orbital magnetoresistance in bismuth. *Phys. Rev. X* **5**, 021022 (2015).
3. Zhu, Z., Collaudin, A., Fauqué, B., Kang, W. & Behnia, K. Field-induced polarization of Dirac valleys in bismuth. *Nat. Phys.* **8**, 89–94 (2011).
4. Kuchler, R., Steinke, L., Daou, R., Brando, M., Behnia, K. & Steglich, F. Thermodynamic evidence for valley-dependent density of states in bulk bismuth. *Nat. Mater.* **13**, 461–465 (2014).
5. Liang, T., Gibson, Q., Ali, M. N., Liu, M., Cava, R. J. & Ong, N. P. Ultrahigh mobility and giant magnetoresistance in the Dirac semimetal Cd_3As_2. *Nat. Mater.* **14**, 280–284 (2015).
6. Gao, W., Zhu, X., Zheng, F., Wu, M., Zhang, J. & Xi, C. et al. A possible candidate for triply degenerate point fermions in trigonal layered $PtBi_2$. *Nat. Commun.* **9**, 3249 (2018).
7. Gao, W., Hao, N., Zheng, F. W., Ning, W., Wu, M. & Zhu, X. et al. Extremely large magnetoresistance in a topological semimetal candidate pyrite PtBi2. *Phys. Rev. Lett.* **118**, 256601 (2017).
8. Liang, T., Lin, J., Gibson, Q., Kushwaha, S., Liu, M. & Wang, W. et al. Anomalous Hall effect in $ZrTe_5$. *Nat. Phys.* **14**, 451–455 (2018).
9. Liu, E., Sun, Y., Kumar, N., Muechler, L., Sun, A. & Jiao, L. et al. Giant anomalous Hall effect in a ferromagnetic kagome-lattice semimetal. *Nat. Phys.* **14**, 1125–1131 (2018).
10. Nakatsuji, S., Kiyohara, N. & Higo, T. Large anomalous Hall effect in a non-collinear antiferromagnet at room temperature. *Nature* **527**, 212–215 (2015).
11. Ali, M. N., Xiong, J., Flynn, S., Tao, J., Gibson, Q. D. & Schoop, L. M. et al. Large, non-saturating magnetoresistance in WTe2. *Nature* **514**, 205–208 (2014).
12. Zhang, S., Wang, Y., Zeng, Q., Shen, J., Zheng, X. & Yang, J. et al. Scaling of Berry-curvature monopole dominated large linear positive magnetoresistance. *Proc. Natl Acad. Sci. USA* **119**, e2208505119 (2022).
13. Huang, X., Zhao, L., Long, Y., Wang, P., Chen, D. & Yang, Z. et al. Observation of the chiral-anomaly-induced negative magnetoresistance in 3D Weyl semimetal TaAs. *Phys. Rev. X* **5**, 031023 (2015).
14. Xiong, J., Kushwaha, S. K., Liang, T., Krizan, J. W., Hirschberger, M. & Wang, W. et al. Evidence for the chiral anomaly in the Dirac semimetal Na_3Bi. *Science* **350**, 413–416 (2015).
15. Kumar, N., Guin, S. N., Felser, C. & Shekhar, C. Planar Hall effect in the Weyl semimetal GdPtBi. *Phys. Rev. B* **98**, 041103(R) (2018).
16. Wu, M., Zheng, G., Chu, W., Liu, Y., Gao, W. & Zhang, H. et al. Probing the chiral anomaly by planar Hall effect in Dirac semimetal Cd_3As_2 nanoplates. *Phys. Rev. B* **98**, 161110(R) (2018).
17. Takatsu, H., Ishikawa, J. J., Yonezawa, S., Yoshino, H., Shishidou, T. & Oguchi, T. et al. Extremely large magnetoresistance in the nonmagnetic metal $PdCoO_2$. *Phys. Rev. Lett.* **111**, 056601 (2013).
18. Ali, M. N., Schoop, L. M., Garg, C., Lippmann, J. M., Lara, E. & Lotsch, B. et al. Butterfly magnetoresistance, quasi-2D Dirac Fermi surface and topological phase transition in ZrSiS. *Sci. Adv.* **2**, e1601742 (2016).
19. Jo, Y. J., Park, J., Lee, G., Eom, M. J., Choi, E. S. & Shim, J. H. et al. Valley-polarized interlayer conduction of anisotropic Dirac fermions in SrMnBi2. *Phys. Rev. Lett* **113**, 156602 (2014).
20. Zheng, G., Zhu, X., Liu, Y., Lu, J., Ning, W. & Zhang, H. et al. Field-induced topological phase transition from a three-dimensional Weyl semimetal to a two-dimensional massive Dirac metal in $ZrTe_5$. *Phys. Rev. B* **96**, 121401(R) (2017).
21. Wang, J., Deng, J., Liang, X., Gao, G., Ying, T. & Tian, S. et al. Spin-flip-driven giant magnetotransport in A-type antiferromagnet NaCrTe2. *Phys. Rev. Mater.* **5**, L091401 (2021).
22. Chen, X. Z., Feng, J. F., Wang, Z. C., Zhang, J., Zhong, X. Y. & Song, C. et al. Tunneling anisotropic magnetoresistance driven by magnetic phase transition. *Nat. Commun.* **8**, 449 (2017).
23. Hodovanets, H., Eckberg, C. J., Campbell, D. J., Eo, Y., Zavalij, P.Y. & Piccoli, P. et al. Anomalous symmetry breaking in the Weyl semimetal CeAlGe. *Phys Rev B* **106**, 235102 (2022).
24. Xu, J., Wu, F., Bao, J. K., Han, F., Xiao, Z. L. & Martin, I. et al. Orbital-flop induced magnetoresistance anisotropy in rare earth monopnictide CeSb. *Nat. Commun.* **10**, 2875 (2019).
25. Lyu, Y.-Y., Han, F., Xiao, Z.-L., Xu, J., Wang, Y.-L. & Wang, H.-B. et al. Magnetization-governed magnetoresistance anisotropy in the topological semimetal CeBi. *Phys. Rev. B* **100**, 180407(R) (2019).
26. Wang, C., Seinige, H., Cao, G., Zhou, J. S., Goodenough, J. B. & Tsoi, M. Anisotropic magnetoresistance in antiferromagnetic Sr_2IrO_4. *Phys. Rev. X* **4**, 041034 (2014).
27. Wang, H., Lu, C., Chen, J., Liu, Y., Yuan, S. L. & Cheong, S.-W. et al. Giant anisotropic magnetoresistance and nonvolatile memory in canted antiferromagnet Sr2lrO4. *Nat. Commun.* **10**, 2280 (2019).

28. Lu, C., Gao, B., Wang, H., Wang, W., Yuan, S. & Dong, S. et al. Revealing controllable anisotropic magnetoresistance in spin-orbit coupled antiferromagnet Sr_2IrO_4. *Adv. Funct. Mater.* **28**, 1706589 (2018).
29. Kim, J.-W., Chun, S. H., Choi, Y., Kim, B. J., Upton, M. H. & Ryan, P. J. Controlling symmetry of spin-orbit entangled pseudospin state through uniaxial strain. *Phys. Rev. B* **102**, 054420 (2020).
30. Ahadi, K., Lu, X., Salmani-Rezaie, S., Marshall, P. B., Rondinelli, J. M. & Stemmer, S. Anisotropic magnetoresistance in the itinerant antiferromagnetic $EuTiO_3$. *Phys. Rev. B* **99**, 041106(R) (2019).
31. Shekhar, C., Kumar, N., Grinenko, V., Singh, S., Sarkar, R. & Luetkens, H. et al. Anomalous Hall effect in Weyl semimetal half-Heusler compounds RPtBi (R= Gd and Nd). *Proc. Natl Acad. Sci. USA* **115**, 9140–9144 (2018).
32. Suzuki, T., Chisnell, R., Devarakonda, A., Liu, Y. T., Feng, W. & Xiao, D. et al. Large anomalous Hall effect in a half-Heusler antiferromagnet. *Nat. Phys.* **12**, 1119–1123 (2016).
33. Chen, J., Li, H., Ding, B., Chen, P., Guo, T. & Xu, X. et al. Unconventional anomalous Hall effect in the canted antiferromagnetic Half-Heusler compound DyPtBi. *Adv. Funct. Mater.* **31**, 2107526 (2021).
34. Chen, J., Li, H., Ding, B., Zhang, H., Liu, E. & Wang, W. Large anomalous Hall angle in a topological semimetal candidate TbPtBi. *Appl. Phys. Lett.* **118**, 031901 (2021).
35. Pavlosiuk, O., Fałat, P., Kaczorowski, D. & Wiśniewski, P. Anomalous Hall effect and negative longitudinal magnetoresistance in half-Heusler topological semimetal candidates TbPtBi and HoPtBi. *APL Mater.* **8**, 111107 (2020).
36. Singha, R., Roy, S., Pariari, A., Satpati, B. & Mandal, P. Magnetotransport properties and giant anomalous Hall angle in the half-Heusler compound TbPtBi. *Phys. Rev. B* **99**, 035110 (2019).
37. Zhang, H., Zhu, Y. L., Qiu, Y., Tian, W., Cao, H. B. & Mao, Z. Q. et al. Field-induced magnetic phase transitions and the resultant giant anomalous Hall effect in the antiferromagnetic half-Heusler compound DyPtBi. *Phys. Rev. B* **102**, 094424 (2020).
38. Zhu, Y., Singh, B., Wang, Y., Huang, C.-Y., Chiu, W.-C. & Wang, B. et al. Exceptionally large anomalous Hall effect due to anticrossing of spin-split bands in the antiferromagnetic half-Heusler compound TbPtBi. *Phys. Rev. B* **101**, 161105(R) (2020).
39. Chen, J., Xu, X., Li, H., Guo, T., Ding, B. & Chen, P. et al. Large anomalous Hall angle accompanying the sign change of anomalous Hall conductance in the topological half-Heusler compound HoPtBi. *Phys. Rev. B* **103**, 144425 (2021).
40. Guo, C. Y., Wu, F., Wu, Z. Z., Smidman, M., Cao, C. & Bostwick, A. et al. Evidence for Weyl fermions in a canonical heavy-fermion semimetal YbPtBi. *Nat. Commun.* **9**, 4622 (2018).
41. Hirschberger, M., Kushwaha, S., Wang, Z., Gibson, Q., Liang, S. & Belvin, C. A. et al. The chiral anomaly and thermopower of Weyl fermions in the half-Heusler GdPtBi. *Nat. Mater.* **15**, 1161–1165 (2016).
42. Chen, J., Li, H., Ding, B., Liu, E., Yao, Y. & Wu, G. et al. Chiral-anomaly induced large negative magnetoresistance and nontrivial π-Berry phase in half-Heusler compounds RPtBi (R=Tb, Ho, and Er). *Appl. Phys. Lett.* **116**, 222403 (2020).
43. Pavlosiuk, O., Kaczorowski, D. & Wiśniewski, P. Negative longitudinal magnetoresistance as a sign of a possible chiral magnetic anomaly in the half-Heusler antiferromagnet DyPdBi. *Phys. Rev. B* **99**, 125142 (2019).
44. Wang, H., Zhou, Z., Ying, J., Xiang, Z., Wang, R. & Wang, A. et al. Large magneto-transverse and longitudinal thermoelectric effects in the magnetic Weyl semimetal TbPtBi. *Adv. Mater.* **35**, 2206941 (2023).
45. Blaha, P., Schwarz, K., Madsen, G., Kvasnicka, D. & Luitz J. WIEN2k: An Augmented Plane Wave Plus Local Orbitals Program for Calculating Crystal Properties. *WIEN2K: An Augmented Plane Wave plus Local Orbitals Program for Calculating Crystal Properties* (Vienna University of Technology, 2001),
46. Perdew, J. P., Burke, K. & Ernzerhof, M. Generalized gradient approximation made simple. *Phys. Rev. Lett.* **77**, 3865 (1996).
47. Bergemann, C., Julian, S. R., Mackenzie, A. P., NishiZaki, S. & Maeno, Y. Detailed topography of the fermi surface of Sr_2RuO_4. *Phys Rev Lett* **84**, 2662–2665 (2000).
48. Bergemann, C., Mackenzie, A. P., Julian, S. R., Forsythe, D. & Ohmichi, E. Quasi-two-dimensional Fermi liquid properties of the unconventional superconductor Sr2RuO4. *Adv. Phys.* **52**, 639–725 (2003).
49. Hussey, N. E., Abdel-Jawad, M., Carrington, A., Mackenzie, A. P. & Balicas, L. A coherent three-dimensional Fermi surface in a high-transitiontemperature superconductor. *Nature* **425**, 814–817 (2003).
50. Balicas, L., Nakatsuji, S., Hall, D., Ohnishi, T., Fisk, Z. & Maeno, Y. et al. Severe Fermi surface reconstruction at a metamagnetic transition in Ca_2-xSr_xRuO_4 (for 0.2 <or=x<or=0.5). *Phys. Rev. Lett.* **95**, 196407 (2005).
51. Sulaev, A., Zeng, M., Shen, S. Q., Cho, S. K., Zhu, W. G. & Feng, Y. P. et al. Electrically tunable in-plane anisotropic magnetoresistance in topological insulator $BiSbTeSe_2$ nanodevices. *Nano Lett.* **15**, 2061–2066 (2015).
52. Wang, Y., Liu, E., Liu, H., Pan, Y., Zhang, L. & Zeng, J. et al. Gate-tunable negative longitudinal magnetoresistance in the predicted type-II Weyl semimetal WTe_2. *Nat. Commun.* **7**, 13142 (2016).
53. Wang, F., Wang, X., Zhao, Y. F., Xiao, D., Zhou, L. J. & Liu, W. et al. Interface-induced sign reversal of the anomalous Hall effect in magnetic topological insulator heterostructures. *Nat. Commun.* **12**, 79 (2021).